



# Quantitative Characterization of Carbide Loss and Correlation with Microstructure and Performance of Plasma-Sprayed NiCr-Cr<sub>3</sub>C<sub>2</sub> Metal Carbide Coatings

Q. Liu<sup>1</sup> · Y. B. Hu<sup>1</sup> · N. J. Chong<sup>1</sup> · Y. Bai<sup>1</sup> · G. Z. Ma<sup>2</sup> · Z. D. Li<sup>3</sup> · M. Y. Bao<sup>3</sup> · H. Zhan<sup>3</sup> · R. J. Wang<sup>3</sup> · Y. W. Sun<sup>1</sup> · Y. Wang<sup>1</sup> · Y. S. Ma<sup>4</sup>

Submitted: 31 May 2020 / in revised form: 22 October 2020 / Accepted: 31 October 2020 / Published online: 3 January 2021  
© ASM International 2021

**Abstract** The aim of this work is to quantitatively describe the carbide loss during plasma deposition of metal carbide coatings and link it to the microstructure and performance of the as-sprayed coatings. To do this, a carbide loss index is defined. The results suggest that the microstructure and performance of such coatings can be tailored by controlling the content of carbides based on the proposed carbide loss index. The size of the particles in flight had the most significant effect on the carbide loss during the processing of the powder in the plasma jet. When the carbide loss index decreased from 0.028 to 0.014, the carbide content in the NiCr-Cr<sub>3</sub>C<sub>2</sub> coating increased from 23.18 to 34.43 vol.%, effectively improving the microhardness of the coating and eliminating the formation of cluster cracks between the carbides and metal binder. In ball-on-disk friction testing with a Si<sub>3</sub>N<sub>4</sub> ball, the coating with the highest content of carbides showed the lowest friction coefficient and best tribological properties. This study provides in-depth understanding of the nature of carbide loss and the factors that affect it under plasma spray conditions.

**Keywords** carbide loss · metal carbide coatings · microhardness · supersonic atmospheric plasma spraying · tribological properties

## Introduction

Thermally sprayed metal carbide coatings are widely applied in numerous applications including wear–erosion–oxidation resistance and surface repair in many industrial environments (Ref 1–4). In these applications, many thermal spraying methods, such as atmospheric plasma spraying (APS), high-velocity oxygen–fuel (HVOF), and high-velocity air–fuel (HVOF) spraying, are employed for coating deposition. Traditional APS with lower velocity of 200–600 m/s and higher jet temperature of 12,000–15,000 K easily results in dissolution of carbides and degradation of the coating performance (Ref 5–7). Compared with APS, the use of various advanced methods such as HVOF or HVOF can effectively prevent such dissolution of carbides and improve the deformability of in-flight particles due to their lower temperature and higher velocity (Ref 8–10). Another important method, supersonic atmospheric plasma spraying (SAPS), can remarkably increase the temperature of the plasma jet and the velocity of in-flight particles by the structural optimization of the spray gun and the internal powder injection process. This method has shown potential to fabricate many high-performance metal carbide coatings (Ref 11–14).

The microstructure and performance of metal carbide coatings are closely related to carbide loss. Such loss caused by decarburization or rebound greatly restricts efforts to improve the coating performance. For NiCr-Cr<sub>3</sub>C<sub>2</sub> metal carbide coatings, some orthorhombic Cr<sub>3</sub>C<sub>2</sub> dissolved into the metal binder is gradually converted to

---

Q. Liu and Y. B. Hu contributed equally to this work.

✉ Y. Bai  
byxjtu@mail.xjtu.edu.cn

✉ G. Z. Ma  
magz0929@163.com

<sup>1</sup> State Key Laboratory for Mechanical Behavior of Materials, Xi'an Jiaotong University, Xi'an 710049, China

<sup>2</sup> National Key Lab for Remanufacturing, Army Academy of Armored Forces, Beijing 100072, China

<sup>3</sup> Beijing Jinlunkuntian Special Machine Co., Ltd, Beijing 100083, China

<sup>4</sup> Wuzhong Instrument Co. Ltd, Wuzhong 751100, China

hexagonal (*P63mc*)  $\text{Cr}_7\text{C}_3$  (Ref 15) and orthorhombic (*Pnma*)  $\text{Cr}_{23}\text{C}_6$  (Ref 16), and the free carbon from these carbides is converted to  $\text{CO}$ ,  $\text{CO}_2$ , or  $\text{CH}_4$  inside or outside the in-flight particles (Ref 17–20). Our previous study found that the  $\text{Cr}_{23}\text{C}_6$  was distributed along the grain boundaries of the metal binder in a network shape, having the potential to gather retained carbides around it to improve the wear resistance during heavy load friction processes (Ref 21). The amorphous and nanocrystalline supersaturated phases are also formed due to the decomposition of elements in carbides, becoming trapped in the metal binder under the rapid solidification of the in-flight particles (Ref 4, 7). Furthermore, a small amount of  $\text{Cr}_2\text{O}_3$  is observed in HVOF-sprayed coatings due to the lack of a protective gas during spraying (Ref 3, 22). In addition, the rebound loss seen in HVOF or HVOF  $\text{NiCr-Cr}_3\text{C}_2$  coatings can be attributed to the fact that some retained carbides located inside the low-temperature particles rebound from the substrate surface after high-velocity impact (Ref 7, 23, 24).

Against this background, carbide loss inevitably occurs during thermal spraying, and the microstructure and performance of metal carbide coatings are highly dependent on its extent. However, the nature of such carbide loss and the related influencing factors are not fully understood at present. Therefore, as a typical metal carbide coating,  $\text{NiCr-Cr}_3\text{C}_2$  was chosen as a research object in the present work. A carbide loss index ( $\text{CL}^*$ ) as a function of the temperature, velocity, size, and standoff distance of in-flight particles was proposed, and its correlation with the microstructure and performance of the coatings was systematically studied with the aim of depositing high-performance metal carbide coatings.

## Experimental Procedures

### Coating Material and Preparation

Spherical, agglomerated, and sintered 25 wt.%  $\text{NiCr-Cr}_3\text{C}_2$  powder (Chengdu Daguang Thermal Spraying Materials Co., Ltd.) with nominal size of 15–45  $\mu\text{m}$  was used to prepare the coatings. The substrate, 2Cr13 stainless steel with size of  $\phi$  25.4 mm  $\times$  10 mm, was ultrasonically cleaned and then grit-blasted prior to coating deposition. Five groups of  $\text{NiCr-Cr}_3\text{C}_2$  coatings were fabricated by using a SAPS system (CYS III-120), and the spraying parameters were optimized using a Box–Behnken design (BBD) method (Table 1). A detailed description of this method can be found in our previous study (Ref 14, 25). Besides, a commercial online system (Spray Watch 2i, Oseir, Finland) was used to monitor the temperature and velocity of in-flight particles. During spraying, a V-shaped

shield with diameter of 1 mm was placed on the polished 2Cr13 stainless steel substrate to collect single splats (Fig. 1).

### Microstructural Characterization

The microstructure and wear scar morphology of the coatings were observed by scanning electron microscopy (SEM, SU3500, Japan), and the corresponding element distribution was analyzed by energy-dispersive spectrometry (EDS, INCA-AE350, Japan). The carbide content and porosity of the as-sprayed coatings were determined by using image analysis software (Image-Pro<sup>®</sup> Plus v 6.0) according to ASME E2109-01 (2014) standard. The average value was determined by randomly selecting ten cross-sectional SEM micrographs at magnification of 500 $\times$ . This method for detecting the carbide content and porosity has been widely employed in previous studies (Ref 4, 22, 24).

The microstructure of as-sprayed coatings was also studied by high-resolution transmission electron microscopy (TEM, JEM-2100Plus, Japan). To obtain TEM samples, two polished coating samples were bonded with epoxy cement, then a cylinder with size of  $\phi$ 3 mm  $\times$  3 mm was cut out from the coating section by wire cutting. Subsequently, the cylindrical sample was ground to less than 80  $\mu\text{m}$  with SiC sandpaper then thinned by argon ion milling (Leica EM RES102). After obtaining selected diffraction TEM images, four diffraction spots were selected and their separation measured using image analysis software (Digital Micrograph). Finally, the crystal plane orientation of these points was calculated and calibrated by using JADE 6.0 software and the formula for the angle between crystal planes.

The phase composition of the feedstock powder and as-sprayed coatings was analyzed by x-ray diffraction (XRD, DMAX-RB 12 kW, Japan) in the range from 30° to 80° with  $\text{Cu K}_\alpha$  ( $\lambda = 1.5418^\circ$ ) radiation at 30 kV, 10 mA, and 0.002°/step. Peak fitting to the XRD patterns was performed using JADE 6.0 software. The chemical composition of the as-sprayed coatings was characterized by x-ray photoelectron spectroscopy (XPS, ESCALAB Xi+, USA) using a monochromatic  $\text{Al K}_\alpha$  source with respect to the C 1s binding energy of carbon at 284.7 eV.

### Microhardness and Wear Performance

The microhardness of the coatings was measured on polished cross-sections by using a Vickers indentation tester (HVS-1000, Yanrun Light Machinery Technology, China) at load of 2.94 N for 15 s. The average microhardness was obtained by repeating the measurement 20 times in different areas.

**Table 1** Spray parameters of as-sprayed NiCr-Cr<sub>3</sub>C<sub>2</sub> coatings

Coating	Spraying power, kW	Voltage, V	Current, A	Argon flow rate, L s <sup>-1</sup>	Standoff distance, mm	Feed rate, g s <sup>-1</sup>
S1	46.2	110	420	2.7	100	0.4
S2	46.2	110	420	3.0	100	0.4
S3	50.4	120	420	3.0	100	0.4
S4	50.4	120	420	3.3	100	0.4
S5	54.6	130	420	3.7	100	0.4

**Fig. 1** Schematic of temperature and velocity detection and collection of single splats through a V-shaped slit

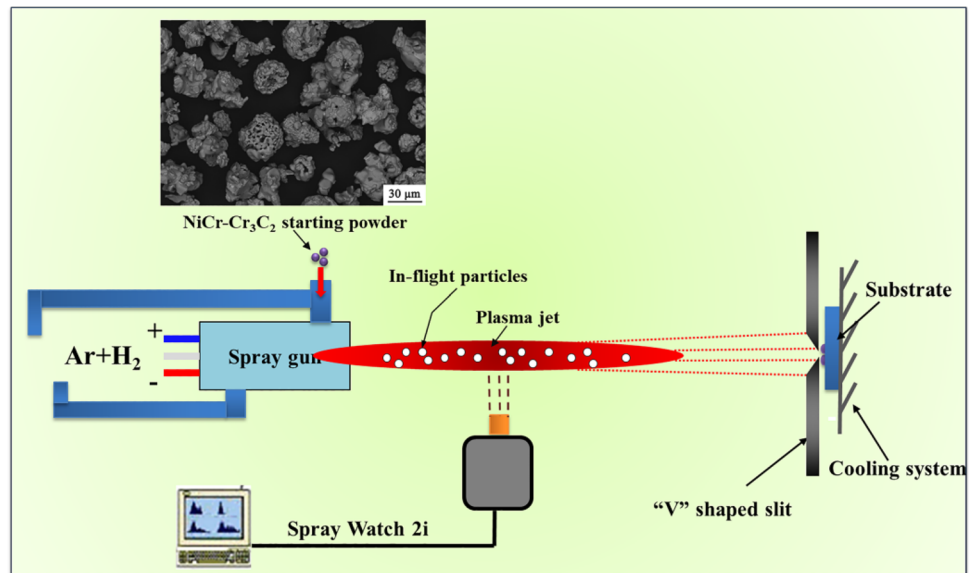


**Table 2** Experimental parameters in friction and wear testing

Load, N	2.0
Friction radius, mm	5.0
Linear velocity, m/s	0.2
Time, s	6000
Friction pair	Si <sub>3</sub> N <sub>4</sub> ball

Rotating ball-on-disk friction and wear testing (HT-1000) was employed to evaluate the wear resistance of the coatings at room temperature, repeating the test on each coating for three times to obtain stable experimental data. The surface of each sample was ground and polished before testing until the surface roughness ( $R_a$ ) was less than 0.8  $\mu\text{m}$  according to ASTM D4066. A commercially available Si<sub>3</sub>N<sub>4</sub> ceramic ball with diameter of 5.95 mm and hardness of 91 HRC was used for the friction pair, and the specific experimental parameters are presented in Table 2. Upon completion of friction and wear testing, the morphology and volume loss of the wear scar were analyzed by three-dimensional (3D) laser confocal microscopy (VK-

9700, Keyence, Japan) and optical 3D surface profilometry (Superview W1, Chotest, China). The wear rate was defined as the change of wear volume per unit wear distance and normal load (Ref 22, 24, 26, 27), expressed as

$$W = \frac{V_w}{N \cdot S} \tag{Eq 2}$$

where  $W$  is the wear rate ( $\text{mm}^3/\text{N}\cdot\text{m}$ ),  $V_w$  is the wear volume ( $\text{mm}^3$ ),  $N$  is normal load (N), and  $S$  is the wear distance (m).

## Results

### Microstructure and Composition of As-Sprayed Coatings

Figure 2 shows the cross-sectional morphology of the as-sprayed NiCr-Cr<sub>3</sub>C<sub>2</sub> coatings. It can be observed that some pores and cracks coexisted in the coatings (Fig. 2a-e, white arrows), and the numbers of cracks and pores in coating S5 were significantly lower than those in other coatings. Many studies (Ref 4, 7, 28-31) have confirmed that the

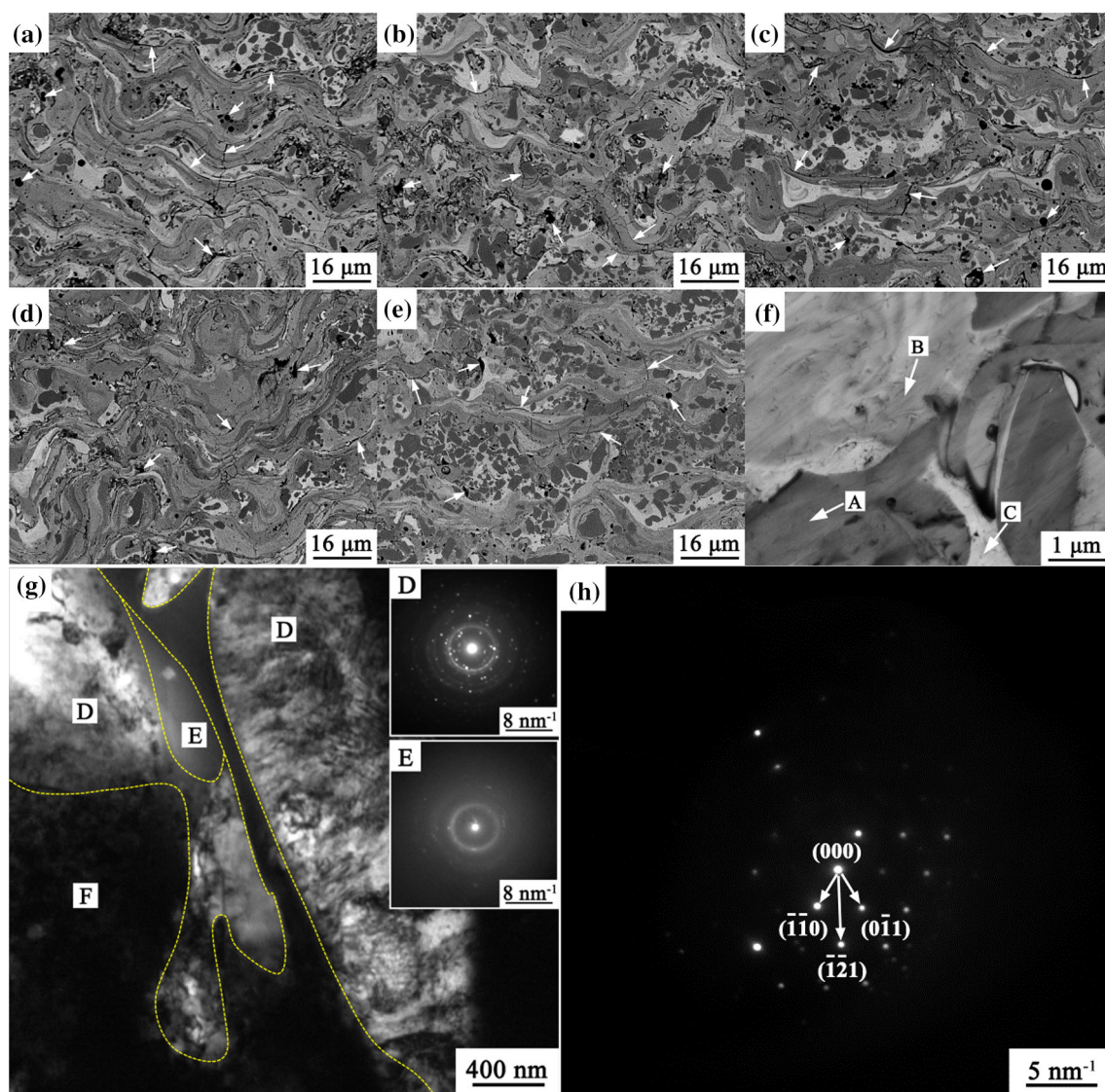


**Fig. 2** Cross-sectional SEM and TEM micrographs of NiCr-Cr<sub>3</sub>C<sub>2</sub> coatings: (a) S1, (b) S2, (c) S3, (d) S4, and (e) S5, and (f) a detailed view of coating S5; (g) TEM image of coating S5; (h) diffraction spot pattern of region F

shortcomings of agglomeration sintering technology result in a distribution of a small amount of pores and microcracks between the hard carbides and metal binder in NiCr-Cr<sub>3</sub>C<sub>2</sub> feedstock powder. Due to the insufficient melting of the metal binder, these microcracks are retained in the as-sprayed coatings and reduce the interphase bonding. Some new microcracks are also initiated by the difference in thermal expansion coefficient between the carbides and metal binder under nonequilibrium solidification conditions. In addition, the preparation of the metallographic specimens may also lead to initiation of microcracks (Ref 7, 21). The formation of pores was caused by the accelerated dissolution of gases in the in-flight particles. In the high-velocity plasma jet, these gases are not fully released

**Table 3** Elemental composition (wt.%) of as-sprayed coating S5

	Ni	Cr	C	Other
Region A	...	85.42	14.58	...
Region B	48.27	40.97	8.98	1.78
Region C	23.01	64.25	12.75	...

during the very short solidification time, thus remaining in the coating (Ref 32).

Based on the SEM images as well as EDS results (Table 3), it can be concluded that the NiCr-Cr<sub>3</sub>C<sub>2</sub> coatings consisted of dark-gray carbides (region A), a gray interfacial transition region (region B), and light-gray metal

binder (region C), as shown in Fig. 2(f). The formation of the interfacial transition region can be explained by the fact that a large number of carbides were fully dissolved into the molten metal binder at high temperatures, and some free carbon from the dissolved carbides gradually diffused from the center of the high-concentration carbides to the surface of the metal binder, thereby forming a low-carbon shell (Ref 4, 20, 33). This concentrated distribution greatly promoted the continuous diffusion of free carbon, thus enhancing the dissolution of carbides and forming a large-area interfacial transition region. The microstructure of coating S5 was further analyzed by transmission electron microscopy (TEM) and corresponding selected-area diffraction patterns (Fig. 2g, h). The results suggested that this coating mainly consisted of polycrystalline (region D), amorphous (region E), and crystal structure (region F). It is well known that a single set of hexahedral diffraction spots can be indexed to a single-crystal structure, while polycrystalline structures contain multiple crystal forms with different sizes, shapes, and orientations, resulting in multiple sets of diffraction spots and even polycrystalline rings. The polycrystalline region contained NiCr, (Ni,Cr)<sub>7</sub>C<sub>3</sub>, Ni-metastable, Cr<sub>23</sub>C<sub>6</sub>, and Cr (or C) from dissolved carbides (Ref 7, 34). Ni-metastable phase was defined as the nanocrystalline nickel binder material containing high concentrations of Cr and C from dissolved carbides. Meanwhile, the formation of amorphous phase was closely related to the nonequilibrium solidification of the metal binder (NiCr). The crystal phase was referred to as carbides, exhibiting orthorhombic structure (*Pnma*) and growing preferentially along  $[\bar{1}\bar{2}1]$  direction.

Figure 3 shows the content of carbides, interface transition region, and metal binder in the NiCr-Cr<sub>3</sub>C<sub>2</sub> coatings. It can be found that coating S5 contained more high-

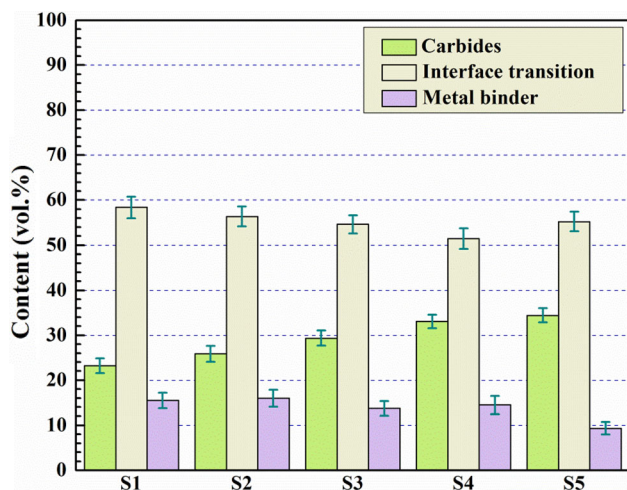


**Fig. 3** Content of carbides, interfacial transition region, and metal binder in NiCr-Cr<sub>3</sub>C<sub>2</sub> coatings

hardness carbides (34.43 vol.%) than the other coatings, which is conducive to improve its microhardness. The high content of interfacial transition region (55.24 vol.%) in coating S5 implies that more sufficient interdiffusion occurred between the carbides and metal binder, which can effectively fill microdefects such as the cracks and pores caused by cracks retained from the original powder and the mismatch of thermal expansion coefficient between the two phases, thereby reducing the porosity and improving the interphase bonding of the coating.

Figure 4 shows the XRD spectra and XPS patterns of the coatings. As seen from Fig. 4(a), the main diffraction peaks could be associated with Cr<sub>3</sub>C<sub>2</sub>, Cr<sub>23</sub>C<sub>6</sub>, NiCr, (Ni,Cr)<sub>7</sub>C<sub>3</sub>, and Ni-metastable phases. The intensity of the peak observed at 39.022°, corresponding to Cr<sub>3</sub>C<sub>2</sub> phase, was the highest for both the feedstock powder and as-sprayed coatings. The intensity of the peak observed at 40.209° was significantly higher for coatings S5 and S4 than for the feedstock powder, suggesting a potential transformation of the preferred growth crystal plane from [121] to [230]. Additionally, according to the ratio of the peak at 40.209° to the highest one (at 39.022°), the relative intensity of Cr<sub>3</sub>C<sub>2</sub> phase in coating S3 (0.85) was significantly lower than for the other coatings (0.91–1.0). These results indicate that decarburization or interdiffusion of carbides occurred to a great extent during spraying. The presence of (Ni,Cr)<sub>7</sub>C<sub>3</sub> with the highest peak intensity further verifies the analysis of the interfacial transition region in Fig. 2(f). Some studies have suggested that the contrast of (Ni,Cr)<sub>7</sub>C<sub>3</sub> phase in SEM images is significantly different from that of carbides or metal binder due to its higher atomic weight (Ref 20, 24). Moreover, the supersaturated network carbides (Cr<sub>23</sub>C<sub>6</sub>) aggregated the retained carbides and further increased the carbide content (Ref 4, 35, 36). Figure 4(b–e) presents the XPS spectra of the NiCr-Cr<sub>3</sub>C<sub>2</sub> coatings. In the full spectrum (Fig. 4b), no remarkable difference was observed among the coatings, indicating that the NiCr-Cr<sub>3</sub>C<sub>2</sub> coatings deposited using in-flight particles with different velocities and temperatures had almost the same chemical composition. Note that the presence of the O 1s peak in the full spectrum is mainly due to the presence of adsorbed oxygen and other oxide impurities on the sample surface, which can be eliminated by argon-ion etching. Figure 4(c) shows the C 1s spectra of the NiCr-Cr<sub>3</sub>C<sub>2</sub> coatings. The characteristic peak consists of three components, corresponding to C–O bond at binding energies of 288.4 and 286.3 eV, C–C bond at a binding energy of 284.7 eV, and Cr–C bond at a binding energy of 282.8 eV. This result further verifies the occurrence of decarburization during spraying. In the Cr 2p spectra of the coatings (Fig. 4d), two characteristic peaks corresponding to 2p<sub>3/2</sub> and 2p<sub>1/2</sub> electrons were deconvoluted into four chemical binding states, being assigned to Cr–C bond

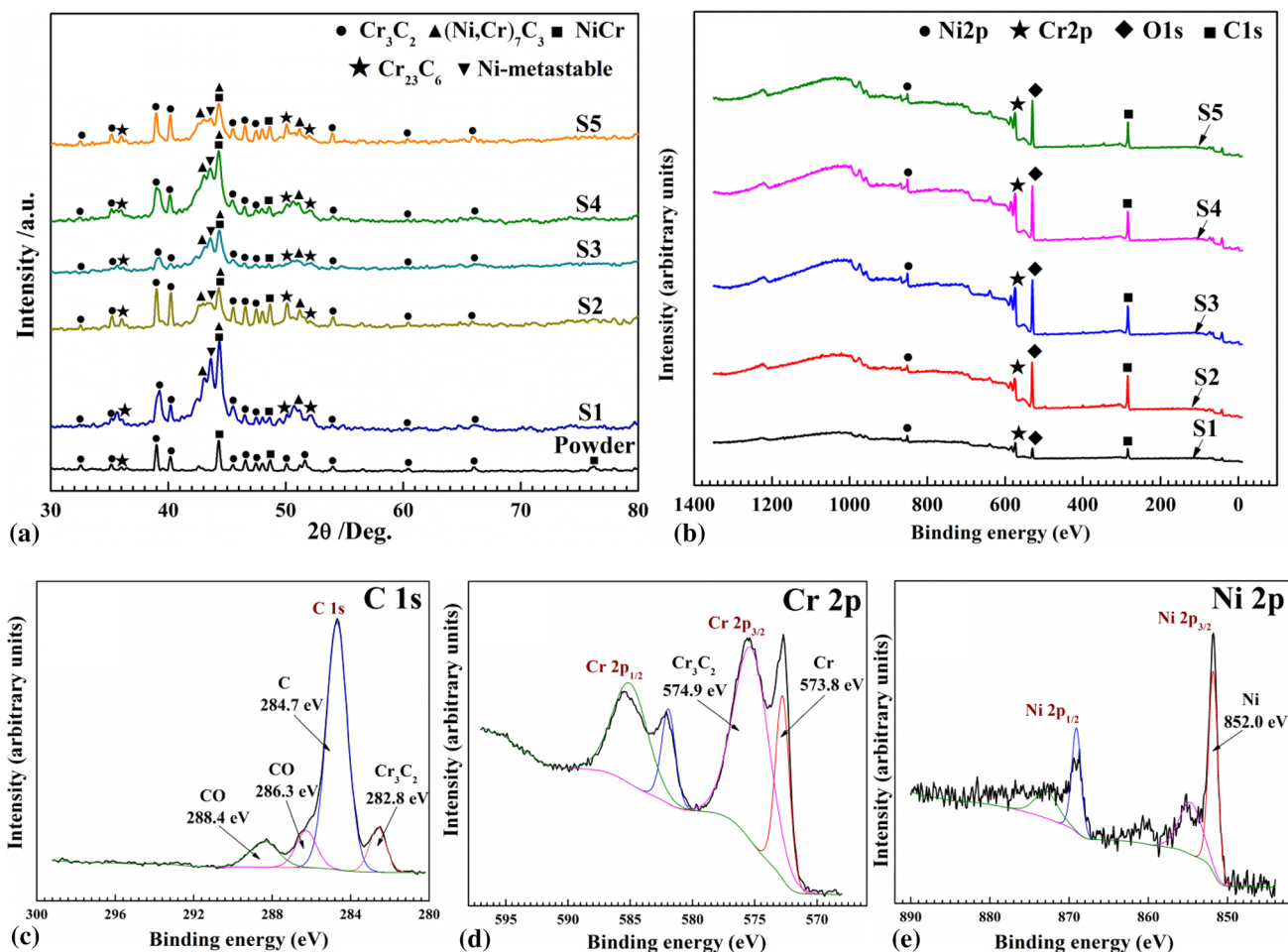


**Fig. 4** (a) XRD and (b) total, (c) C 1s, (d) Cr 2p, and (e) Ni 2p XPS patterns of as-sprayed NiCr-Cr<sub>3</sub>C<sub>2</sub> coatings

(binding energy 574.9 eV) and Cr–Cr bond (binding energy 573.8 eV) (Ref 37). In the Ni 2p spectra (Fig. 4e), the coating exhibited one characteristic peak corresponding to 2p<sub>3/2</sub> and 2p<sub>1/2</sub> electrons at binding energy of 852.0 eV, considered to correspond to Ni–Ni bond. The formation of Cr–Cr and Ni–Ni bonds occurs due to agglomeration and sintering of the original powder.

### Carbide Loss Index

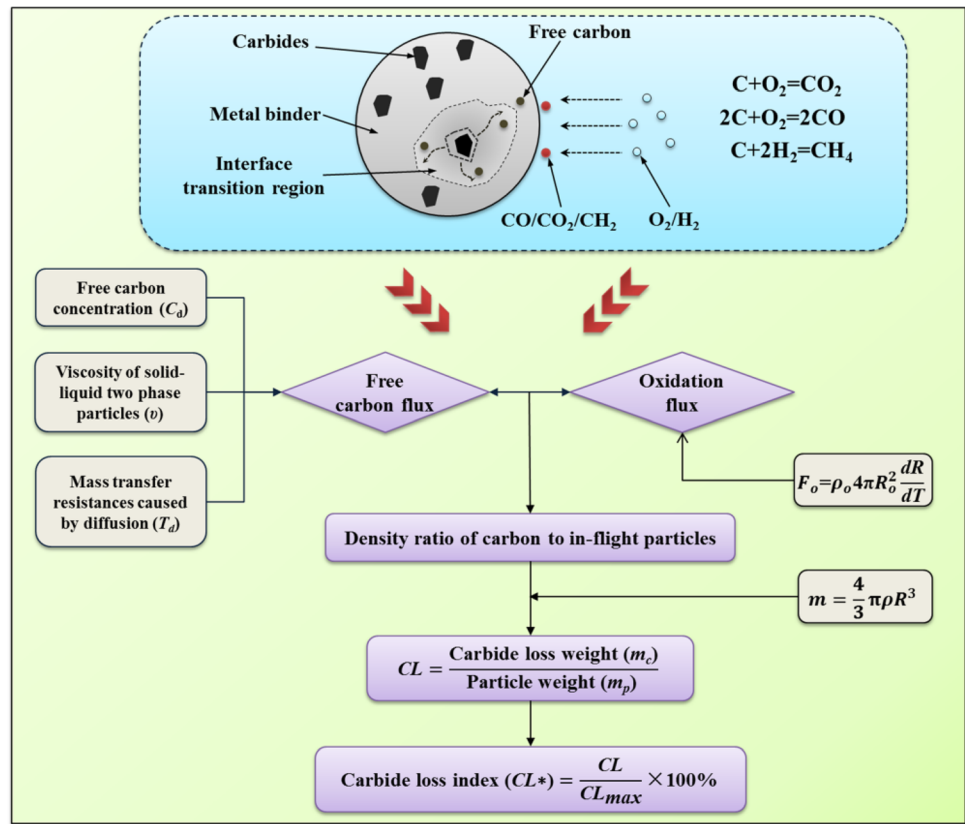
During the preparation of NiCr-Cr<sub>3</sub>C<sub>2</sub> coatings, most of the carbides that dissolve into the metal binder precipitate in the form of Cr<sub>23</sub>C<sub>6</sub> under the nonequilibrium solidification conditions, while only a small amount of carbides separate in the form of carbon. These free carbon atoms are gradually consumed by the reaction between free carbon and gas (O<sub>2</sub> or H<sub>2</sub>) inside or outside the in-flight particles, eventually resulting in carbide loss due to decarburization. The rebound loss caused by the low temperature and high velocity of the in-flight particles can be ignored. Similar to the oxidation index of Xiong et al. (Ref 38), in this study, a

physical parameter named the carbide loss index is proposed to analyze the carbide loss behavior; the corresponding schematic diagram is shown in Fig. 5. As seen from Fig. 5, the free carbide concentration and the mass transfer resistance were regarded as the main factors affecting the reaction between carbon and gas phase. In addition, the influence of the viscosity on the diffusion behavior of free carbon in the two-phase solid–liquid particles was also considered. Therefore, the relationship between the free carbon flux ( $F_c$ ) and the carbide flux ( $F_o$ ) caused by the reaction can be expressed as

$$F_c = \frac{C_d}{T_d v} = F_o \frac{M_c}{M_o}, \quad (\text{Eq 3})$$

where  $T_d$  is the mass transfer resistance caused by diffusion,  $v$  is the viscosity of the two-phases solid–liquid in-flight particles (Ref 39),  $C_d$  is the concentration of free carbon (Ref 40), and  $M_c$  and  $M_o$  are the atomic weights of free carbon and carbides due to the decarburization reaction, respectively. The detailed formulas for these parameters are listed as follows:

**Fig. 5** Schematic diagram of carbide loss index derivation



$$v = \frac{\vartheta_o}{1 - V}, \tag{Eq 4}$$

$$T_d = \frac{1}{4\pi\rho_p D_c} \left( \frac{1}{R_c} - \frac{1}{R_p} \right), \tag{Eq 5}$$

$$F_o = \rho_o 4\pi R_o^2 \frac{dR}{dT}, \tag{Eq 6}$$

$$C_d = C_o \left[ 1 - a \exp\left(-\frac{bD_c T}{R_p}\right) \right], \tag{Eq 7}$$

$$\frac{4}{3}\pi R_p^3 = \pi R^2 h, \tag{Eq 8}$$

where  $\vartheta_o$  is the viscosity of the metal binder ( $\vartheta_o = 0.0097 \exp(4620/T)$ ),  $V$  is the volume fraction of carbide reinforcement within the in-flight particle ( $V \approx 75 \text{ vol.}\%$ ),  $\rho_o$  is the density of carbides formed by decarburization,  $\rho_p$  is the density of the in-flight particles,  $D_c$  is the diffusion coefficient of free carbon (Ref 41) ( $D_c = 2.6 \times 10^{-12} \text{ m}^2/\text{s}$ ),  $C_o$  is the carbide concentration at the beginning of decarburization,  $a$  and  $b$  are coefficients ( $a = 0.811$  and  $b = -2.467$ ) (Ref 40),  $T$  is the in-flight time ( $T = D/\int_0^t v_p(t)dt = 2D/v_p$ , where  $D$  is the standoff distance), and  $R$  and  $h$  are the radius and thickness of the flattened particles after impact on the substrate, respectively.  $R_o$ ,  $R_c$ , and  $R_p$  are the radius of oxygen, free carbon,

and in-flight particles, respectively ( $R_o = 7.4 \times 10^{-11} \text{ m}$ ;  $R_c = 7.7 \times 10^{-11} \text{ m}$ ). Substituting Eq 4-8 into Eq 3, the relationship between the free carbon flux ( $F_c$ ) and the carbide flux ( $F_o$ ) caused by the reaction can be expressed as

$$4\pi\rho_o \frac{M_c}{M_o} \int R_o^2 dR = \frac{(1 - V)C_o}{4\pi\rho_p D_c \left( \frac{1}{R_c} - \frac{1}{R_p} \right)} \int \left[ 1 - a \exp\left(-\frac{bD_c T}{R_p}\right) \right] dT. \tag{Eq 9}$$

Integration and development of Eq 9 yields the following density relationship between carbides caused by reaction and in-flight particles:

$$\frac{\rho_c}{\rho_p} = \frac{6DA(1 - V)}{R_c^2 \vartheta_o v_p \left( 1 - \frac{R_c}{R_p} \right)} C_o \left[ 1 + a \frac{2bD_c D}{v_p R_p^2} \exp\left(-\frac{2bDD_c}{v_p R_p^2}\right) \right], \tag{Eq 10}$$

where  $A$  is a constant ( $A = M_o D_c / M_c$ ). Therefore, the ratio of the carbide loss weight ( $m_c$ ) to the weight of a single in-flight particle ( $m_p$ ) can be expressed as

$$\begin{aligned}
 CL &= \frac{m_c}{m_p} \\
 &= \frac{6AD(1-V)}{v_p \vartheta_o R_p^2 \left( \frac{R_c}{R_p} - 1 \right)} C_o \left[ 1 + a \frac{2bD_c D}{v_p R_p^2} \exp \left( - \frac{2bDD_c}{v_p R_p^2} \right) \right].
 \end{aligned}
 \tag{Eq 11}$$

Furthermore, the carbide loss index can be calculated as the ratio of  $m_c$  to  $m_p$  under different conditions, expressed as

$$CL^* = \frac{CL}{CL_{\max}}, \tag{Eq 12}$$

where  $CL_{\max}$  is defined as the ratio of  $m_c$  to  $m_p$  when the carbides are completely eliminated by decarbonization. Note that  $CL_{\max}$  is a critical value that is tightly dependent on the process parameters and that can increase or decrease depending on the thermal spraying method applied. Therefore, the key to obtaining  $CL_{\max}$  is to determine the critical values of several key parameters that affect CL. In this study, it is found from Eq 11 that CL decreases with increase of the velocity and size of the in-flight particles, but increases with increase of the temperature or standoff distance. A temperature of the in-flight particles above the boiling point ensures complete decarburization and decomposition of the carbides, thus the temperature used to calculate  $CL_{\max}$  is the boiling point temperature of carbides ( $Cr_3C_2$ ) up to 4073 K. Comparing various thermal spraying methods used for metal-carbide coatings, the velocity (200–600 m/s) of APS is generally lower than that of other spraying methods (HVOF, HVAF, and SAPS) (Ref 3, 7), while the standoff distance (200–430 mm) of HVOF or HVAF is significantly greater than that of APS or SAPS

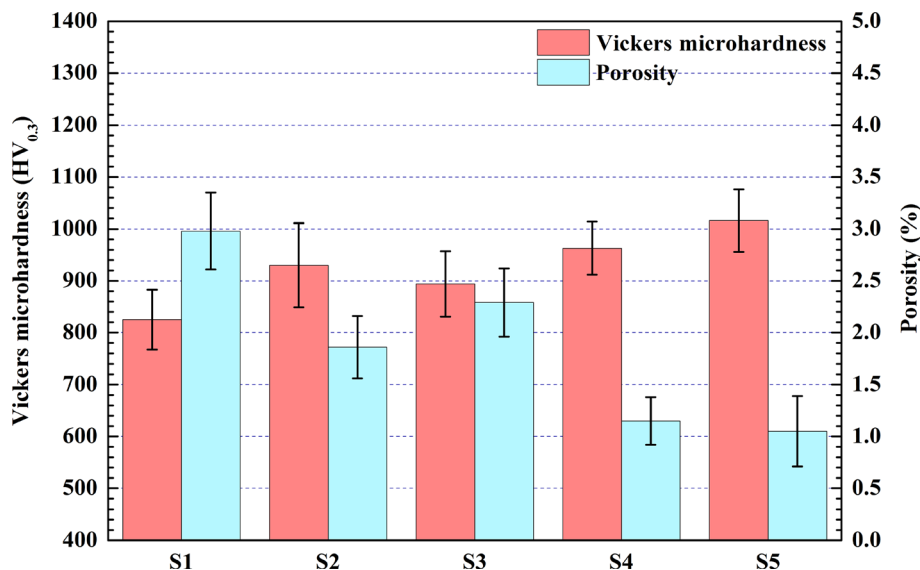
(80–150 mm) (Ref 3, 9, 24, 42–45), thus the minimum velocity of 200 m/s and maximum standoff distance of 430 mm were selected for the calculation of  $CL_{\max}$ . In addition, due to the wide application and preference for powder size of 15–45  $\mu m$  in the field of metal carbide coating deposition, the minimum particle size of  $CL_{\max}$  was set to be 15  $\mu m$ .

### Microhardness and Wear Performance of Coatings

Figure 6 shows the microhardness and porosity of the as-sprayed NiCr- $Cr_3C_2$  coatings. It is seen that coating S5 had higher microhardness ( $1016 \pm 60$  HV<sub>0.3</sub>) and lower porosity ( $1.05 \pm 0.34\%$ ) compared with the other coatings. In addition, coating S1 showed the lowest microhardness ( $825 \pm 58$  HV<sub>0.3</sub>) and highest porosity ( $2.98 \pm 0.37\%$ ). It was worth noting that the microhardness of coating S5 was higher than most coatings deposited using other processes (Ref 3, 6, 22, 24, 27, 43, 45–48).

Figure 7 shows the results for the friction coefficient and wear rate. As seen from Fig. 7(a), the friction coefficient of coating S2 lay in the range from 0.94 to 0.98, while coating S5 showed the lowest friction coefficient (0.6–0.7). According to the results in Fig. 7(b), coating S5 showed the lowest average friction coefficient (0.65) and lowest wear rate ( $9.80 \times 10^{-5}$  mm<sup>3</sup>/N·m). The SEM and 3D morphology of the wear scars revealed the same characteristics for the NiCr- $Cr_3C_2$  coatings, including abrasive grooves and a small number of cracks (Fig. 8). Therefore, the main wear mechanism of the coatings was associated with abrasive wear (Ref 9, 22, 24). Note that adhesion of wear debris containing Si and O elements was also observed on

**Fig. 6** Microhardness and porosity of as-sprayed NiCr- $Cr_3C_2$  coatings





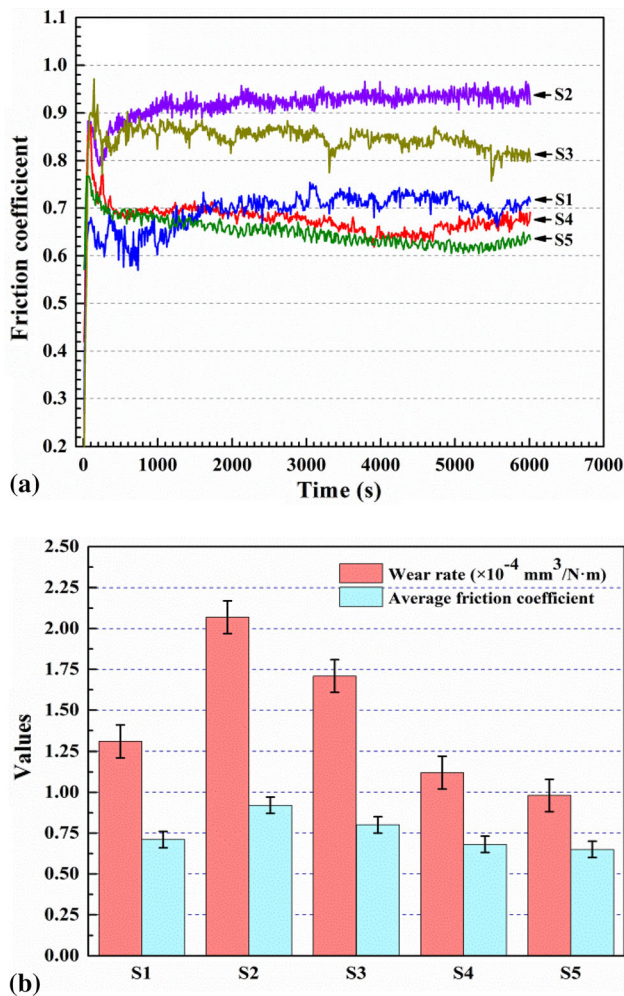


Fig. 7 Curves of (a) friction coefficient and (b) average friction coefficient and wear rate of NiCr-Cr<sub>3</sub>C<sub>2</sub> coatings

the wear scars (Fig. 9), indicating debris transferred during friction and wear.

### Discussion

Based on the above results, CL\* was employed to quantitatively evaluate and control the carbide loss of the metal carbide coatings during SAPS spraying, thereby reducing the carbide loss and optimizing the microstructure and tribological properties. To verify the applicability of CL\*, the CL\* value of the NiCr-Cr<sub>3</sub>C<sub>2</sub> coatings was calculated according to Eq 11, Eq 12, and the physical parameters given in Table 4, and the variation of CL\* and carbide content was compared and analyzed (Fig. 10). It was found that a high content of carbides resulted in a low CL\*. Compared with the other coatings, coating S5 exhibited a lower CL\* (0.014) and higher carbide content (34.43 vol.%), while the CL\* and carbide content of coating S1

only reached 0.028 and 23.18 vol.%, respectively. Because the calculation results for CL\* were consistent with the variation trend of the carbide content inside the coatings, the carbide loss during spraying can be effectively and accurately evaluated and predicted using CL\*.

The effect of the spray parameters on the calculated value of CL\* was further predicted by adjusting parameters such as the temperature, velocity, standoff distance, and size of the in-flight particles according to Eq 11, and the most critical factor affecting CL\* was also determined. The theoretical prediction results are shown in Fig. 11. It can be seen from Fig. 11(a) that CL\* decreased by approximately 70% as the velocity of the in-flight particles increased from 200 to 650 m/s, because the high velocity significantly shortened the dwell time of the in-flight particles in the plasma jet, thus reducing the decomposition of dissolved carbides and slowing the reaction with the gas phase, which thus resulted in a decrease of CL\*. However, high temperature caused excessive melting of carbides and serious decarburization, resulting in an increase of CL\* by more than 75%. Figure 11(b) shows the influence of the standoff distance and in-flight particle size on CL\* at given temperature and velocity, revealing that, when the size of the in-flight particles was less than 30 μm, CL\* increased from 0.069 to 0.422 as the standoff distance was increased from 70 to 430 mm. Many studies (Ref 25, 49-51) have found that, with an increase of the standoff distance, the velocity of the plasma jet gradually decreases to become close to or even lower than the velocity of in-flight particles under atmospheric drag, thus resulting in a reverse drag force of the plasma jet on the in-flight particles. Therefore, increasing the standoff distance reduces the kinetic energy by prolonging the dwell time of the in-flight particles in atmosphere, thus delaying the nonequilibrium solidification and resulting in full decarburization and decomposition of the carbides. However, when the particle size reaches 30 μm, CL\* decreases from 0.422 to 0.016, which is greater than the reduction effect of the velocity on CL\*. In other words, a size of 30 μm for the in-flight particles can be regarded as the critical value to effectively reduce CL\*. In this study, because the size of the in-flight particles was in the range of 20-30 μm, the influence of their size on CL\* was more significant than that of the other parameters. Therefore, although the higher temperature of the in-flight particles used to deposit coating S5 increased the value of CL\*, the larger particle size ( $R_p = 11.22 \mu\text{m}$ ) had a more significant effect in reducing it, thus the final CL\* was the lowest (0.014).

The coating formed by the accumulation of in-flight particles with low CL\* contained more carbides, not only resulting in the increase of the microhardness of the coating from  $825 \pm 58 \text{ HV}_{0.3}$  to  $1016 \pm 60 \text{ HV}_{0.3}$  but also promoting the formation of an interfacial transition region,

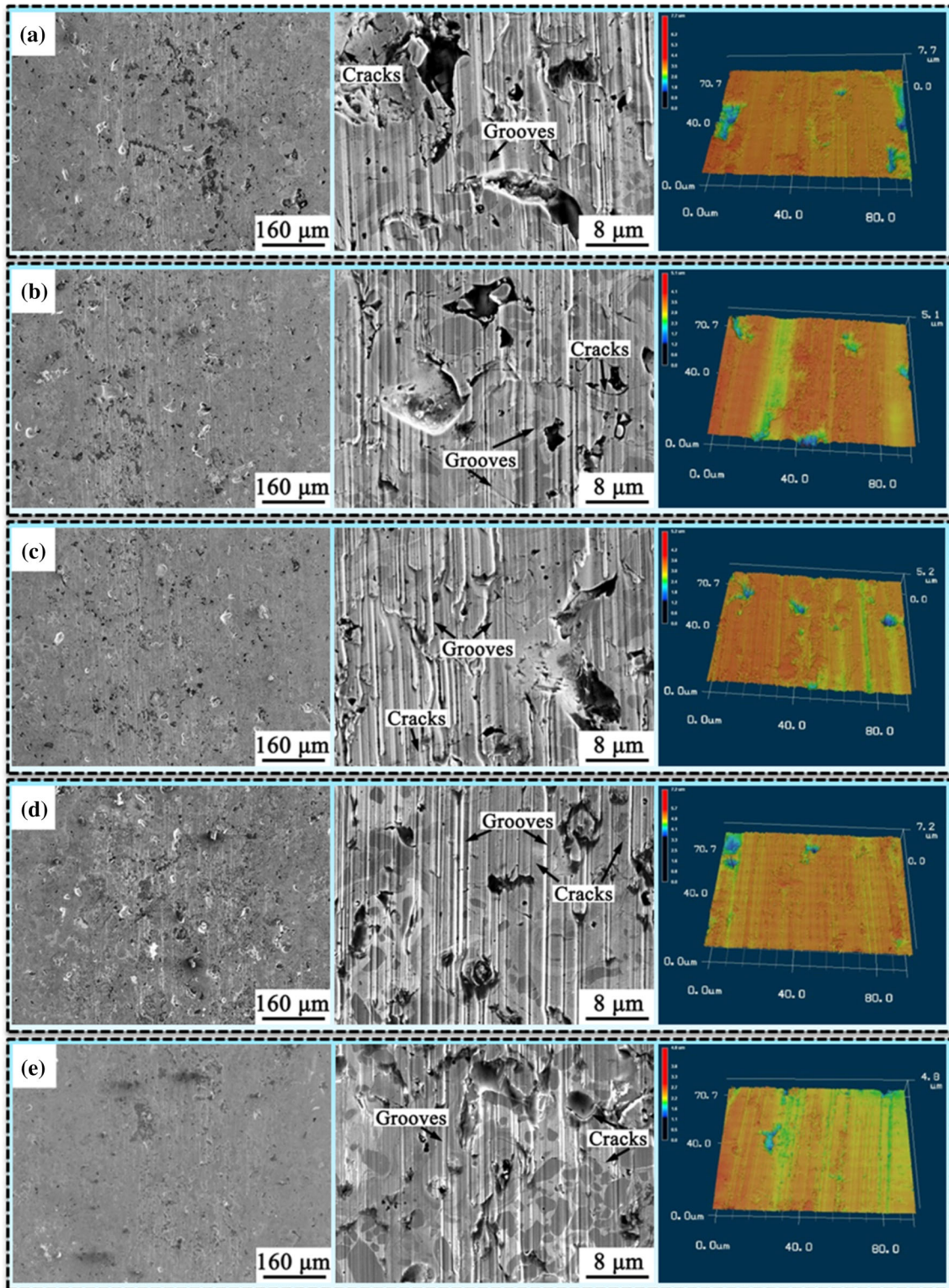


**Fig. 8** Tribological properties and 3D morphology of coating (a) S1, (b) S2, (c) S3, (d) S4, and (e) S5

usually showing a complex microstructure due to the dissolution of carbides under nonequilibrium solidification conditions. These interfacial transition regions effectively

eliminated the microdefects and improved the interphase bonding as well as density of the as-sprayed coatings. The phase composition of the interfacial transition region was

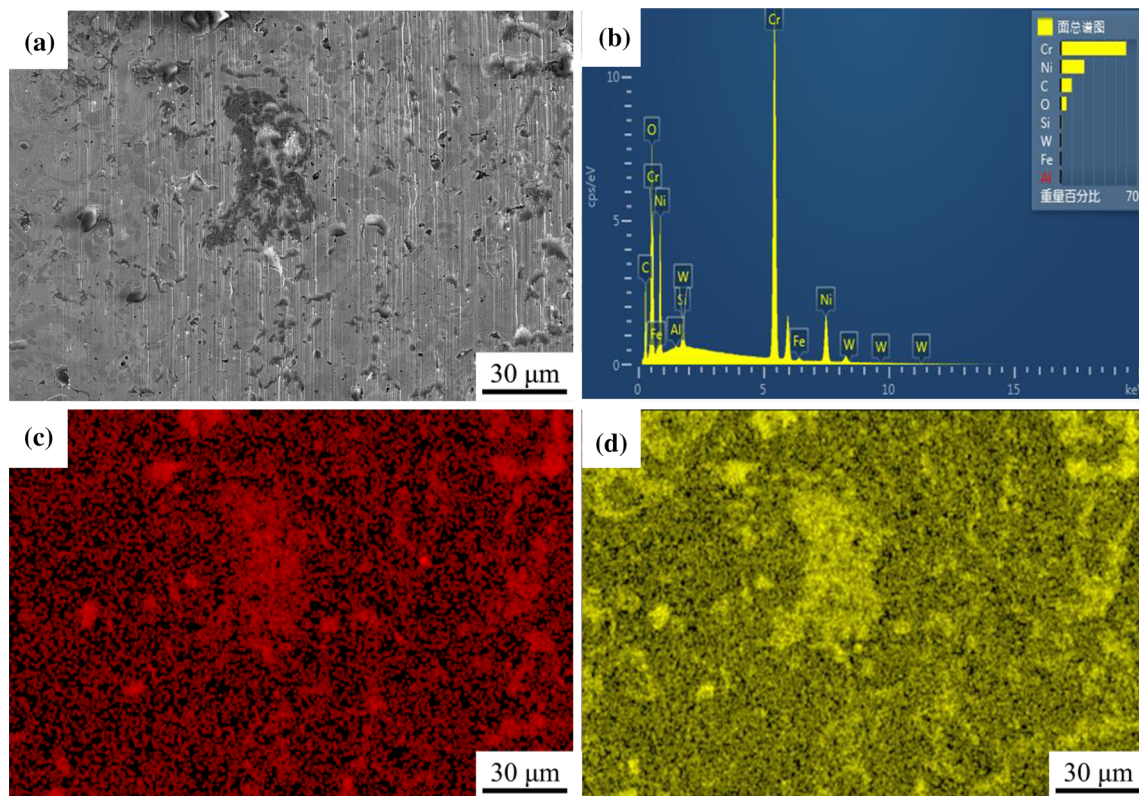


**Fig. 9** Morphology and EDS elemental mapping of wear scars of coating S5: (a) secondary-electron image of wear scars and (b) corresponding EDS spectra; distribution of (c) Si and (d) O elements on wear scars

**Table 4** Physical parameters of supersonic in-flight NiCr-Cr<sub>3</sub>C<sub>2</sub> particles

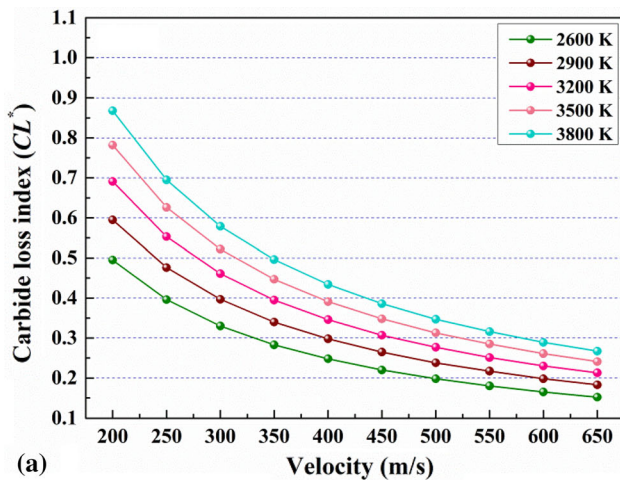
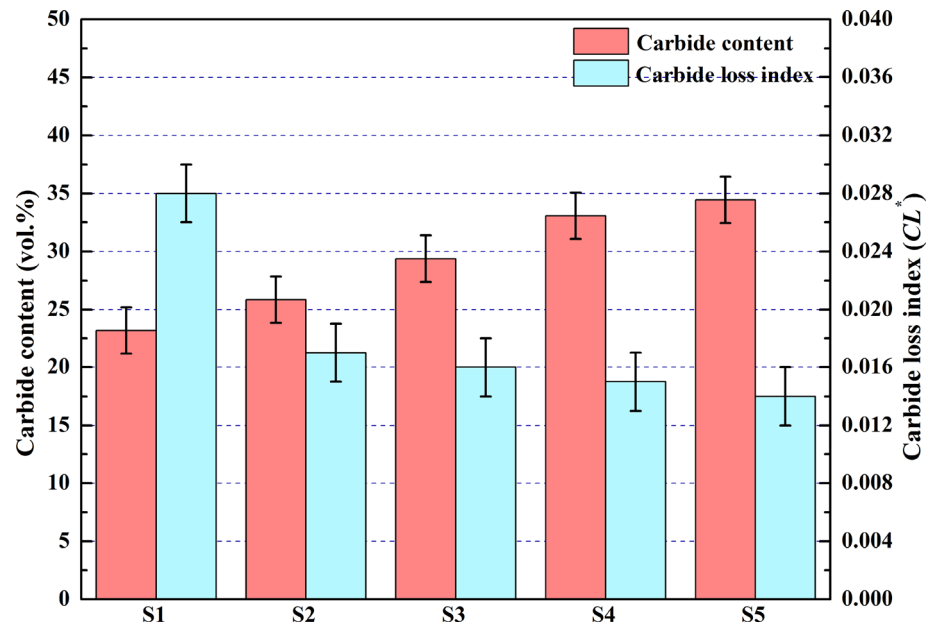
	S1	S2	S3	S4	S5
<i>T</i> , K	2676 ± 3	2636 ± 8	2698 ± 6	2713 ± 3	2959 ± 6
<i>v<sub>p</sub></i> , m s <sup>-1</sup>	492.6 ± 7.4	512.2 ± 6.4	543.7 ± 8.5	560.2 ± 9.2	598.8 ± 8.4
<i>R</i> , μm	38.09	39.79	44.84	50.36	62.46
<i>R<sub>p</sub></i> , μm	9.02	10.50	10.61	10.73	11.22
<i>h</i> , μm	1.04	0.975	0.792	0.725	0.682
<i>v<sub>o</sub></i> , Pa s	0.055	0.056	0.054	0.053	0.046

defined as a combination of amorphous phase, Cr<sub>3</sub>C<sub>2</sub>, Cr<sub>23</sub>C<sub>6</sub>, Ni-metastable, and (Ni,Cr)<sub>7</sub>C<sub>3</sub> according to the XRD analysis.

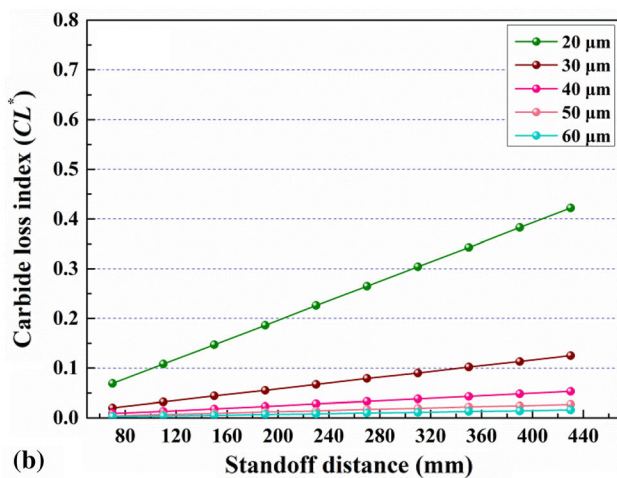
During dry friction testing with a Si<sub>3</sub>N<sub>4</sub> ball, the low-hardness metal binder on the surface of the coatings was first removed by cutting, then the high-hardness carbides protected the metal binder between carbides from further wear via the pinning effect, thus improving the wear resistance of the coatings. Therefore, the carbide content and interphase bonding were the key factors improving the wear resistance of the coatings. Higher carbide content indicates that the coating had higher microhardness and better protective effect on the metal binder, effectively reducing the wear rate. The interphase bonding was dependent on the original content of cluster microcracks

around the carbides or metal binder. Such cracks can initiate and propagate along the interface between carbides, resulting in separation of the carbides from the metal binder to enable serious three-body abrasive wear. In this study, coating S5 contained more carbides and interfacial transition region than the other coatings, indicating that the carbide content and interphase bonding were simultaneously increased, thus it showed the lowest average friction coefficient (0.65) and wear rate ( $9.80 \times 10^{-5}$  mm<sup>3</sup>/N m) among all the coatings. However, the low velocity of the in-flight particles increased their dwell time in the plasma jet and slowed the nonequilibrium solidification behavior, thus increasing the dissolution of carbides and reducing the content of network carbides (Cr<sub>23</sub>C<sub>6</sub>) while forming coating S2 with low microhardness. Besides, the high content

**Fig. 10** Carbide loss index and carbide content of as-sprayed coatings



(a)



(b)

**Fig. 11** Theoretical prediction of variation of carbide loss index with (a) temperature and velocity ( $R_p = 7.5 \mu\text{m}$ ,  $D = 430 \text{ mm}$ ) and (b) size of particles and standoff distance ( $v_p = 200 \text{ m/s}$ ,  $T = 4300 \text{ K}$ )

of metal binder suggested that a lot of original cluster microcracks were present in coating S2, thus reducing the interphase bonding. Therefore, coating S2 showed the highest average friction coefficient (0.92) and wear rate ( $2.07 \times 10^{-4} \text{ mm}^3/\text{N m}$ ) in all the coatings.

## Conclusions

A carbide loss index ( $CL^*$ ) is proposed to quantitatively describe the carbide loss behavior of plasma-sprayed metal carbide coatings, and its influence on the microstructure and tribological properties of coatings was comparatively studied. The following main conclusions can be drawn:

1.  $CL^*$  can be employed to quantitatively evaluate and control the carbide loss behavior of in-flight particles under given spraying parameters and powder properties. The main factors that significantly affected  $CL^*$  are the velocity, temperature, and size of the in-flight particles and the standoff distance.
2.  $CL^*$  can be effectively decreased by increasing the velocity or reducing the temperature, which can well explain why high-velocity spraying methods such as HVOF and SAPS can deposit metal carbide coatings with higher carbide content. In addition, the size of the in-flight particles showed a more significant effect on the reduction of  $CL^*$  than other parameters such as the velocity, temperature, and standoff distance.
3. With a decrease of  $CL^*$  from 0.028 to 0.014, the content of carbides and metal binder in the coatings increased by 11.25 vol.% and decreased by 6.14 vol.%, respectively. This not only improved the

microhardness of the coatings, but also eliminated the original cluster microcracks, thus enhancing the inter-phase bonding.

4. During dry friction testing with a  $\text{Si}_3\text{N}_4$  ball, more carbide and less metal binder inside the metal carbide coatings effectively protected the metal binder from further wear and prevented three-body abrasive wear, thus significantly decreasing the friction coefficient and resulting in better wear performance.

**Acknowledgment** This work was supported by National Key R&D Program of China (Grant No. 2018YFB2004004), Collaborative Innovation Center of Advanced Control Valve Project (Grant No. WZYB-XTX-001), National Natural Science Foundation of China (Grant No. 52005388), China Postdoctoral Science Foundation (Grant No. 2019M653598), and Natural Science Foundation of Shaanxi Province (Grant Nos. 2019TD-020 and 2019JQ-586).

## References

1. J.M. Yuan, T.S. Dong, B.G. Fu, G.L. Li, L. Liu, and R. Wang, Effect of Tungsten Inert Gas Arc Remelting on Microstructure and Wear Properties of Plasma-Sprayed NiCr-Cr<sub>3</sub>C<sub>2</sub> Coating, *J. Mater. Eng. Perform.*, 2019, **28**, p 6320-6329
2. L. Janka, J. Norpoth, R. Trache, and L.M. Berger, Influence of Heat Treatment on the Abrasive Wear Resistance of a Cr<sub>3</sub>C<sub>2</sub>-NiCr Coating Deposited by an Ethene-Fuelled HVOF Spray Process, *Surf. Coat. Technol.*, 2016, **291**, p 444-451
3. L. Lin, G.L. Li, H.D. Wang, J.J. Kang, Z.L. Xu, and H.J. Wang, Structure and Wear Behavior of NiCr-Cr<sub>3</sub>C<sub>2</sub> Coatings Sprayed by Supersonic Plasma Spraying and High Velocity Oxy-Fuel Technologies, *Appl. Surf. Sci.*, 2015, **356**, p 383-390
4. S. Matthews, Development of High Carbide Dissolution/Low Carbon Loss Cr<sub>3</sub>C<sub>2</sub>-NiCr Coatings by Shrouded Plasma Spraying, *Surf. Coat. Technol.*, 2014, **258**, p 886-900
5. Y.X. Cao, Effects of hBN Content on the Microstructure and Properties of Atmospheric Plasma-Sprayed NiCr/Cr<sub>3</sub>C<sub>2</sub>-hBN Composite Coatings, *J. Therm. Spray Technol.*, 2016, **25**(4), p 650-659
6. H.B. Wang, H. Li, H.B. Zhu, F.J. Cheng, D.P. Wang, and Z.X. Li, A Comparative Study of Plasma Sprayed TiB<sub>2</sub>-NiCr and Cr<sub>3</sub>C<sub>2</sub>-NiCr Composite Coatings, *Mater. Lett.*, 2015, **153**, p 110-113
7. S. Matthews, A. Asadov, S. Ruddell, and L.M. Berger, Thermally Induced Metallurgical Processes in Cr<sub>3</sub>C<sub>2</sub>-NiCr Thermal Spray Coatings as a Function of Carbide Dissolution, *J. Alloys Compd.*, 2017, **728**, p 445-463
8. A.S.M. Ang, H. Howse, S.A. Wade, and C.C. Berndt, Development of Processing Windows for HVOF Carbide-Based Coatings, *J. Therm. Spray Technol.*, 2016, **25**, p 28-35
9. G. Bolelli, B. Bonferroni, J. Laurila, L. Lusvarghi, A. Milanti, K. Niemi, and P. Vuoristo, Micromechanical Properties and Sliding Wear Behaviour of HVOF-Sprayed Fe-Based Alloy Coatings, *Wear*, 2012, **276–277**, p 29-47
10. N. Vashishtha, R.K. Khatirkar, and S.G. Sapate, Tribological Behaviour of HVOF Sprayed WC-12Co, WC-10Co-4Cr and Cr<sub>3</sub>C<sub>2</sub>-25NiCr Coatings, *Tribol. Int.*, 2017, **105**, p 55-68
11. H.H. Xi, P.F. He, H.D. Wang, M. Liu, S.Y. Chen, Z.G. Xing, G.Z. Ma, and Z.L. Lv, Microstructure and Mechanical Properties of Mo Coating Deposited by Supersonic Plasma Spraying, *Int. J. Refract. Met. Hard Mater.*, 2020, **86**, p 105095
12. Q.Y. Hou, X.Y. Ma, R.C. Lu, W. Wang, P. Wang, and Z.Y. Huang, Microstructure and Laser Irradiation Characteristics of TiC-Free and TiC-Doped Tungsten-Based Coatings Prepared by Supersonic Atmospheric Plasma Spraying, *Surf. Coat. Technol.*, 2019, **358**, p 796-805
13. Q.Y. Hou, H.Q. Huang, D.H. Zhou, P. Wang, Q. Xie, and Z.Y. Huang, Influence of NbC-Doping on the Microstructure and Thermo-Mechanical Properties of Tungsten Coating Fabricated by Supersonic Atmospheric Plasma Spraying, *Surf. Coat. Technol.*, 2020, **394**, p 125823
14. Y. Bai, L. Zhao, Y. Wang, D. Chen, B.Q. Li, and Z.H. Han, Fragmentation of In-Flight Particles and Its Influence on the Microstructure and Mechanical Property of YSZ Coating Deposited by Supersonic Atmospheric Plasma Spraying, *J. Alloys Compd.*, 2015, **632**, p 794-799
15. F. Herstein and J. Snyman, Identification of Eckstrom-Adcock Iron Carbide as Fe<sub>7</sub>C<sub>3</sub>, *Inorg. Chem.*, 1964, **3**, p 894-896
16. A. Bowman, G. Arnold, E. Storms, and N. Nereson, The Crystal Structure of Cr<sub>23</sub>C<sub>6</sub>, *Acta Crystallogr. B*, 1972, **28**, p 3102-3103
17. D.A. Stewart, P.H. Shipway, and D.G. McCartney, Microstructural Evolution in Thermally Sprayed WC-Co Coatings: Comparison Between Nanocomposite and Conventional Starting Powders, *Acta Mater.*, 2000, **48**, p 1593-1604
18. J.H. He and E.J. Lavernia, Precipitation Phenomenon in Nanostructured Cr<sub>3</sub>C<sub>2</sub>-NiCr Coatings, *Mater. Sci. Eng. A*, 2001, **301**, p 69-79
19. J. Wang, K. Li, D. Shu, X. He, B.D. Sun, Q.X. Guo, M. Nishio, and H. Ogawa, Effects of Structure and Processing Technique on the Properties of Thermal Spray WC-Co and NiCrAl/WC-Co Coatings, *Mater. Sci. Eng. A*, 2004, **371**, p 187-192
20. S. Matthews and L.M. Berger, Inter-Diffusion Between Thermally Sprayed Cr<sub>3</sub>C<sub>2</sub>-NiCr Coatings and an Alloy 625 Substrate during Long-Term Exposure at 500°C, 700°C and 900°C, *J. Alloys Compd.*, 2017, **770**, p 1078-1099
21. Q. Liu, Y. Bai, H.D. Wang, G.Z. Ma, M. Liu, C.Y. Chu, Y.W. Sun, W. Fan, F. Ding, B. Zhao, and Y.T. Wang, Microstructural Evolution of Carbides and Its Effect on Tribological Properties of SAPS or HVOF Sprayed NiCr-Cr<sub>3</sub>C<sub>2</sub> Coatings, *J. Alloys Compd.*, 2019, **803**, p 730-741
22. V. Matikainen, G. Bolelli, H. Koivuluoto, P. Sassatelli, L. Lusvarghi, and P. Vuoristo, Sliding Wear Behaviour of HVOF and HVAF Sprayed Cr<sub>3</sub>C<sub>2</sub>-Based Coatings, *Wear*, 2017, **388–389**, p 57-71
23. C.J. Li, G.C. Ji, Y.Y. Wang, and K. Sonoya, Dominant Effect of Carbide Rebounding on the Carbon Loss During High Velocity Oxy-Fuel Spraying of Cr<sub>3</sub>C<sub>2</sub>-NiCr, *Thin Solid Films*, 2002, **419**, p 137-143
24. G. Bolelli, L.M. Berger, T. Börner, H. Koivuluoto, V. Matikainen, L. Lusvarghi, C. Lyphout, N. Markocsan, P. Nylén, P. Sassatelli, R. Trache, and P. Vuoristo, Sliding and Abrasive Wear Behaviour of HVOF- and HVAF-Sprayed Cr<sub>3</sub>C<sub>2</sub>-NiCr Hardmetal Coatings, *Wear*, 2016, **358–359**, p 32-50
25. K. Liu, J.J. Tang, Y. Bai, Q.Z. Yang, Y. Wang, Y.X. Kang, L. Zhao, P. Zhang, and Z.H. Han, Particle In-Flight Behavior and Its Influence on the Microstructure and Mechanical Property of Plasma Sprayed La<sub>2</sub>Ce<sub>2</sub>O<sub>7</sub> Thermal Barrier Coatings, *Mater. Sci. Eng. A*, 2015, **625**, p 177-185
26. L.Z. Du, C.B. Huang, W.G. Zhang, T.G. Li, and W. Liu, Preparation and Wear Performance of NiCr/Cr<sub>3</sub>C<sub>2</sub>-NiCr/hBN Plasma Sprayed Composite Coating, *Surf. Coat. Technol.*, 2011, **205**, p 3722-3728
27. E. Gariboldi, L. Rovatti, N. Lecis, L. Mondora, and G.A. Mondora, Tribological and Mechanical Behaviour of Cr<sub>3</sub>C<sub>2</sub>-NiCr Thermally Sprayed Coatings after Prolonged Aging, *Surf. Coat. Technol.*, 2016, **305**, p 83-92

28. L.M. Berger, Application of Hardmetals as Thermal Spray Coatings, *Int. J. Refract. Metals Hard Mater.*, 2015, **49**, p 350-364
29. E.L. Cantera and B. Mellor, Fracture Toughness and Crack Morphologies in Eroded WC-Co-Cr Thermally Sprayed Coatings, *Mater. Lett.*, 1998, **37**, p 201-210
30. A.L. Robertson and K.W. White, Microscale Fracture Mechanisms of a Cr<sub>3</sub>C<sub>2</sub>-NiCr HVOF Coating, *Mater. Sci. Eng. A*, 2017, **688**, p 62-69
31. S. Matthews, B. James, and M. Hyland, Microstructural Influence on Erosion Behavior of Thermal Spray Coatings, *Mater. Charact.*, 2007, **58**, p 59-64
32. Y. Wang, Y. Bai, K. Wu, J. Zhou, M.G. Shen, W. Fan, H.Y. Chen, Y.X. Kang, and B.Q. Li, Flattening and Solidification Behavior of In-Flight Droplets in Plasma Spraying and Micro/Macro-Bonding Mechanisms, *J. Alloys Compd.*, 2019, **784**, p 834-846
33. S. Matthews, Compositional Development as a Function of Spray Distance in Unshrouded/Shrouded Plasma Sprayed Cr<sub>3</sub>C<sub>2</sub>-NiCr Coatings, *J. Therm. Spray Technol.*, 2014, **24**, p 515-533
34. M. Gell, E.H. Jordan, Y.H. Sohn, D. Goberman, L. Shaw, and T.D. Xiao, In-flight Oxidation of High-Alloy Steels During Plasma Spraying, *Surf. Coat. Technol.*, 2001, **146–147**, p 48-54
35. F. Otsubo, H. Era, T. Uchida, and K. Kishitake, Properties of Cr<sub>3</sub>C<sub>2</sub>-NiCr Cermet Coating Sprayed by High Power Plasma and High Velocity Oxy-Fuel Processes, *J. Therm. Spray Technol.*, 2000, **9**(4), p 499-504
36. O.M. Cintho, E.A.P. Favilla, and J.D.T. Capocchi, Mechanical-Thermal Synthesis of Chromium Carbides, *J. Alloys Compd.*, 2007, **439**, p 189-195
37. T. Wang, G. Zhang, and B. Jiang, Comparison in Mechanical and Tribological Properties of CrTiAlMoN and CrTiAlN Nanomultilayer Coatings Deposited by Magnetron Sputtering, *Appl. Surf. Sci.*, 2016, **363**, p 217-224
38. H.B. Xiong, L.L. Zheng, L. Li, and A. Vaidya, Melting and Oxidation Behavior of In-flight Particles in Plasma Spray Process, *Int. J. Heat Mass Transf.*, 2005, **48**, p 5121-5133
39. C.J. Li, Y.Y. Wang, G.J. Yang, A. Ohmori, and K.A. Khor, Effect of Solid Carbide Particle Size on Deposition Behaviour, Microstructure and Wear Performance of HVOF Cermet Coatings, *Mater. Sci. Technol.*, 2004, **20**, p 1087-1096
40. P. Marini and G. Abbruzzese, Decarburization Rate Related to Surface Oxidation of Grain Oriented Silicon Steel, *J. Magn. Magn. Mater.*, 1982, **26**, p 15-21
41. W.J. Quadackers, R. Schulten, K. Bongartz, and H. Nickel, Mathematical Modeling for Carbon Diffusion and Carbide Precipitation in NiCr-Based Alloys, *Key Eng. Mater.*, 1991, **20–28**, p 1737-1746
42. E. Mayrhofer, L. Janka, W.P. Mayr, J. Norpoth, M.P. Ripoll, and M. Gröschl, Cracking Resistance of Cr<sub>3</sub>C<sub>2</sub>-NiCr and WC-Cr<sub>3</sub>C<sub>2</sub>-Ni Thermally Sprayed Coatings under Tensile Bending Stress, *Surf. Coat. Technol.*, 2015, **281**, p 169-175
43. K. Bobzin, L. Zhao, M. Öte, T. Königstein, and M. Steeger, Impact Wear of an HVOF-Sprayed Cr<sub>3</sub>C<sub>2</sub>-NiCr Coating, *Int. J. Refract. Met. Hard Mater.*, 2018, **70**, p 191-196
44. S. Hong, Y.P. Wu, B. Wang, Y.G. Zheng, W.W. Gao, and G.Y. Li, High-Velocity Oxygen-Fuel Spray Parameter Optimization of Nanostructured WC-10Co-4Cr Coatings and Sliding Wear Behavior of the Optimized Coating, *Mater. Des.*, 2014, **55**, p 286-291
45. W.L. Chen, T.J. Mao, B.Y. Zhang, S.H. Zhang, and X.N. Meng, Designs and Preparation of Advanced HVOF-PVD Duplex Coating by Combination of HVOF and Arc Ion Plating, *Surf. Coat. Technol.*, 2016, **304**, p 125-133
46. J.K.N. Murthy and B. Venkataraman, Abrasive Wear Behavior of WC-CoCr and Cr<sub>3</sub>C<sub>2</sub>-20 (NiCr) Deposited by HVOF and Detonation Spray Processes, *Surf. Coat. Technol.*, 2006, **200**, p 2642-2652
47. M.A. Zavareh, A.A.D.M. Sarhan, B.B. Razak, and W.J. Basirun, The Tribological and Electrochemical Behavior of HVOF-Sprayed Cr<sub>3</sub>C<sub>2</sub>-NiCr Ceramic Coating on Carbon Steel, *Ceram. Int.*, 2015, **41**, p 5387-5396
48. T. Varis, T. Suhonen, O. Caloniun, J. Čuban, and M. Pietola, Optimization of HVOF Cr<sub>3</sub>C<sub>2</sub>-NiCr Coating for Increased Fatigue Performance, *Surf. Coat. Technol.*, 2016, **305**, p 123-131
49. M. Krauss, D. Bergmann, U. Fritsching, and K. Bauckhage, In-situ Particle Temperature, Velocity and Size Measurements in the Spray Forming Process, *Mater. Sci. Eng. A*, 2002, **326**, p 154-164
50. M. Friis, P. Nylén, C. Persson, and J. Wigren, Investigation of Particle In-flight Characteristics During Atmospheric Plasma Spraying of Yttria-Stabilized ZrO<sub>2</sub>: Part. 1 Experimental, *J. Therm. Spray Technol.*, 2001, **10**, p 301-310
51. Y. Bai, L. Zhao, Y.M. Qu, Q.Q. Fu, Y. Wang, K. Liu, J.J. Tang, B.Q. Li, and Z.H. Han, Particle In-flight Behavior and Its Influence on the Microstructure and Properties of Supersonic-Atmospheric-Plasma-Sprayed Nanostructured Thermal Barrier Coatings, *J. Alloys Compd.*, 2015, **644**, p 873-882

**Publisher's Note** Springer Nature remains neutral with regard to jurisdictional claims in published maps and institutional affiliations.